ADVANCED FUNCTIONAL MATERIALS
www.afm-journal.de

Optimizing Light-Harvesting Polymers via Side Chain Engineering

Peng Liu, Sheng Dong, Feng Liu, Xiaowen Hu, Liqian Liu, Yaocheng Jin, Shengjian Liu, Xiong Gong, Thomas P. Russell,* Fei Huang,* and Yong Cao*

A series of conjugated polymers using naphtho[1,2-c:5,6-c]bis[1,2,5]thiadiazole and benzodithiophene alternating backbone is synthesized to investigate the effect of side chain substitution on conjugated donor–acceptor polymer on electronic, morphological, and photovoltaic properties. It is found that light absorption and frontier energy levels of the resultant polymers are strongly affected by the side chains. The thin film morphology, crystal structure, crystallinity, and orientation also depend on the side chains; the side chain type affects more in the π–π stacking direction, while the side chain density plays a significant role in the lamellar packing direction. The thickness of the active layer also influences the performance of the solar cells with some materials showing enhanced performance with thicker active layers. The best solar cell device in this study has power conversion efficiencies of 8.14%, among the highest in materials of similar structure.

1. Introduction

The performance of plastic solar cells has shown a continuous increase over the last decade, due to a systematic development of new materials to suit specific requirements in devices by matching energy levels and optimizing morphologies.[1–4] Semiconducting π-conjugated polymers made of donor–acceptor (D–A) hybrids are still leading the development, which show facile tuning of band gaps and energy levels by introducing new or different constituent units.[5,6] However, in comparison to the development of new conjugated building blocks, modifying side chains offers an alternative, perhaps more convenient and cost-effective route to optimize materials.[7–18] Modifying side chain constituents is usually done in a framework of an established high-performance backbone with the aim of fine tuning the morphology. The selection of side chain substituents, usually alkyl units, needs to balance polymer solubility with the ability for the main chains to self-assemble into ordered units. Polymers with bulky side chains have good solubility in organic solvents for processing, and less bulky side chains provide good interchain packing that ensures charge-carrier transport in solid films. Using advanced structural characterization tools, a number of recent studies have shown the importance of side chain tuning. For example, Beaujuge et al. showed that side chains can influence the polymer self-assembly and preferential crystalline orientation;[19] Cho et al. demonstrated that the solubility, energy level, light absorption, surface tension, and intermolecular packing of the resulting polymers could be changed by altering the functional groups of side chains;[20] Osaka et al. found that the backbone orientation can be changed by tuning the length between adjacent side chains;[21,22] McGehee et al. studied the molecular interactions between polymer segments and fullerenes using linear and branched side chains.[23] Each of these parameters strongly affects the morphology and power conversion efficiencies (PCEs) of photovoltaic devices. There is no universal guidance to select the chemical constitution of the ideal side chains. From the viewpoint of solubility, longer linear alkyl chains afford comparable solubility to shorter, branched alkyl substituents.[9] From the molecular ordering viewpoint, linear side chains will promote π–π stacking between the backbones, leading to better charge transport and, usually, higher short circuit currents (J_{sc}).[10] However, strong intermolecular interactions can lead to greater dark currents (J_{so}) that reduce the open circuit voltage (V_{oc}).[14] Consequently, there is a delicate balance that needs to be struck to generate conjugated polymers with a suitable mixture of linear and branched side

P. Liu, S. Dong, X. Hu, L. Liu, Y. Jin, S. Liu, Prof. F. Huang, Prof. Y. Cao
Institute of Polymer Optoelectronic Materials and Devices
State Key Laboratory of Luminescent Materials and Devices
South China University of Technology
Guangzhou 510640, P. R. China
E-mail: msfhuang@scut.edu.cn
Dr. F. Liu
Materials Sciences Division
Lawrence Berkeley National Lab
Berkeley, CA 94720, USA
E-mail: iamfengliu@gmail.com
Dr. X. Hu, Prof. X. Gong
Department of Polymer Engineering
The University of Akron
250 South Forge Street
Akron, OH 44325-0301, USA
Prof. T. P. Russell
Department of Polymer Science and Engineering
University of Massachusetts
Amherst, MA 01003, USA
E-mail: russell@mail.pse.umass.edu

DOI: 10.1002/adfm.201501878

chains that afford an intermediate π–π stacking distance, good carrier transport, high V_{oc}, and J_{sc}, which are critical for device performance.[14,24]

We have recently developed a double benzothiadiazole (BT)-fused heterocycle, naphtho[1,2-c:5,6-c′]bis[1,2,5]thiadiazole (NT), which was introduced into the conjugated polymer to promote light harvesting.[25] NT is a strong electron acceptor, which strongly affects the energy levels of the resultant polymers; the enlarged aromatic plane enhances the π–π stacking of the polymer chains with improved carrier mobility, which makes it a promising building block for the copolymers used in photovoltaic devices, especially in thick active-layer devices.[26–30] When polymerized with benzodithiophene (BDT), the polymer, {4,8-bis(4,5-didecyl-2-thienyl)-benzo[1,2-b:4,5-b′] dithiophene-alt-[4,9-bis(4-hexyl-2-thienyl)-naphtho[1,2-c:5,6-c′] bis[1,2,5]thiadiazole-5,5-diyl]} (PBDT-DTNT), showed a high PCE of 8.62% at the thickness of 280 nm and maintained a high efficiency of 7.24% when the thickness was increased to 1 μm.[31] In this report, the alkyl side chain optimization of PBDT-DTNT was investigated by modulating the type and density of the alkyl substituents. We synthesized a series of D–A copolymers, varying only the linear or branched side chains on the BDT or DTNT units (**Scheme 1**). Less bulky substituents resulted in insoluble polymers in organic solvents (Supporting Information). The photovoltaic performance of these polymers in polymer solar cell (PSC) was good, with PCEs ranging from ≈5.5% to ≈8.0%. After optimizing processing solvent and active layer thickness, polymer PC6/dC10-based devices showed a PCE of 8.14% at a thickness of 250 nm. Detailed structural analysis of these polymers in the bulk heterojunction (BHJ) films was performed using grazing incidence X-ray diffraction (GIXD), atomic force microscope (AFM), and resonant soft X-ray scattering (RSoXS) to elucidate the influence of varied side chains on the polymer ordering, film morphology and the corresponding photovoltaic performance.

2. Results and Discussion

2.1. Material Synthesis

The synthetic routes used to prepare the five polymers are shown in **Scheme 2**. Detailed synthesis procedures are described in the Experimental Section. Polymers were synthesized via Stille polycondensation using the DTNT (**8**) and BDT (**3** or **6**) building blocks. The π-conjugated backbone structure was the same for all these polymers and the influence of the side chains were compared. All the five polymers showed good solubility in common organic solvents while their analogues with less bulky side chains precipitated during the polymerization in less than 2 h and were not soluble in common solvents, such as chloroform and chlorobenzene (CB). The five polymers had molecular weights from 20 to 30 kg mol^{-1}, which are quite high for low band gap polymers. It is reported that the molecular weight of the polymers would influence the photovoltaic properties by altering the aggregation behavior.[32,33] In the current case, all polymers had reasonably high molecular weights, which provided a useful platform to be focused on comparing the structure–property relationship by side chain variations. The thermal properties of these polymers were studied by thermal gravimetric analysis (TGA) and differential scanning colorimetry (DSC). All the polymers showed good thermal stability up to 400 °C (before degradation), with no detectable endotherms or exotherms seen by DSC (TGA and DSC results are shown in the Supporting Information).

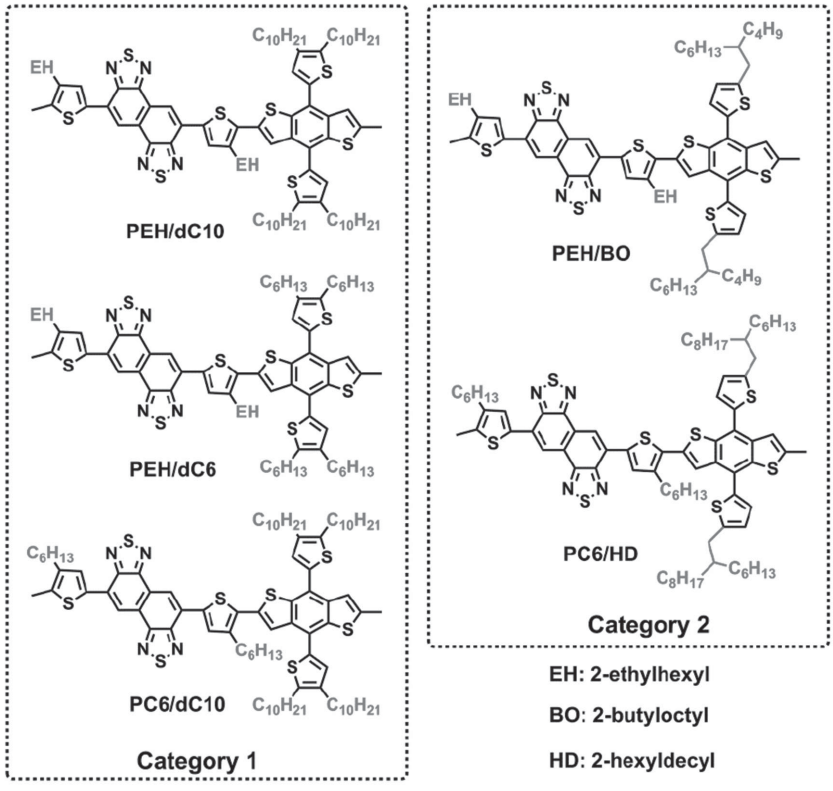

Scheme 1. Structure of the polymers based on BDT-DTNT backbone with varied side chains. Left column: polymers with high side chain density; right column: polymers with low side chain density.

2.2. Optical and Electrochemical Properties

The UV–vis absorption spectra of the polymers in dilute CB solutions and thin films are shown in **Figure 1**a,b, and the data are summarized in **Table 1**. All the polymers showed two characteristic absorption bands, similar to many D–A conjugated copolymers, where the short wavelength absorption originated from the π–π^* transition of the main chain chromophore and the long wavelength absorption was ascribed to the intramolecular charge transfer (ICT) between the BDT and NT segments. The five polymers can be separated into two categories: (1) dilinear substitution on BDT thiophene units with high side chain density

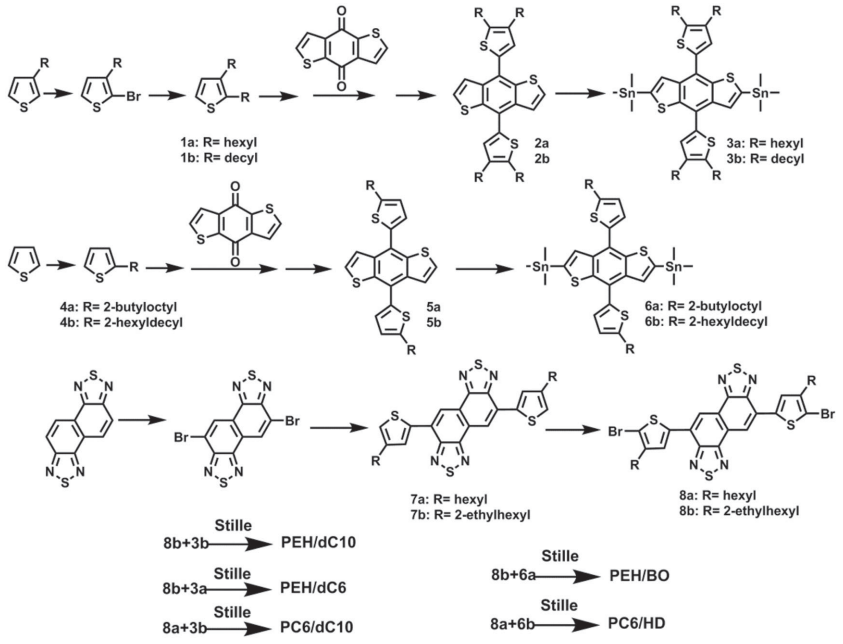

Scheme 2. The synthetic route of the polymers and detailed steps can be found in the Supporting Information.

and (2) monobranched substitution on BDT thiophene units with low side chain density. In solution, the disubstituted polymer PEH/dC10 showed an absorption peak at 602 nm and a weak shoulder at 645 nm was observed. Reducing the chain length of the substituted alkyls on BDT (PEH/dC6) led to a new shoulder at an even longer wavelength region (≈715 nm). Using linear short alkyl chains on the NT units (PC6/dC10) improved molecular aggregation, showing in the intensity growth of the mid-wavelength (≈665 nm) and long wavelength (≈720 nm) peaks (Figure 1a). Using monosubstituted alkyl chains on BDT units also affects absorption strongly. For PEH/BO, an absorption peak at 568 nm was seen and a long wavelength region absorption at ≈705 nm was observed. The PC6/HD polymer showed an absorption peak at 584 nm and two shoulders at 650 and 710 nm. From solution to thin film, the absorption profile of these polymers changed significantly. The short wavelength absorption peak (around or below 600 nm) disappeared

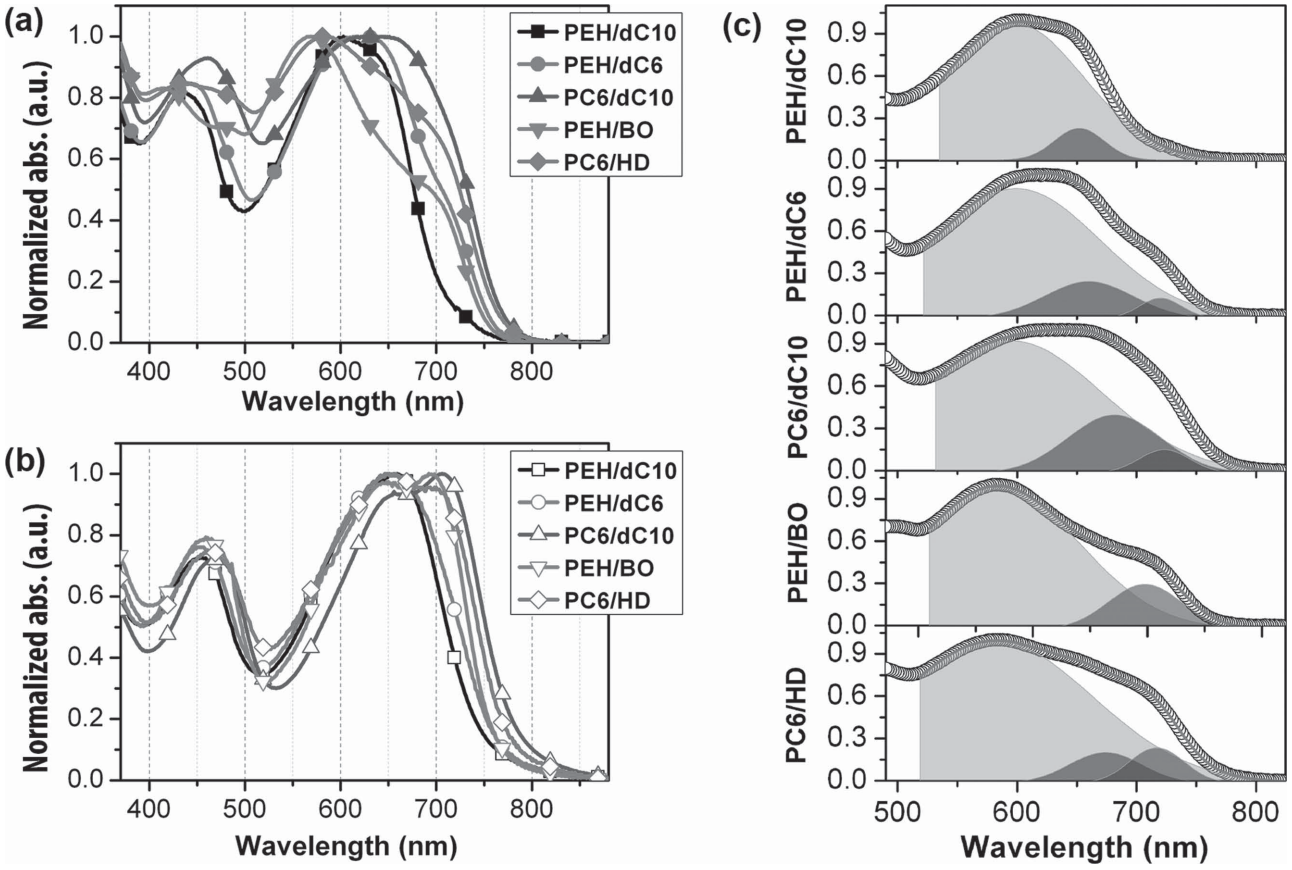

Figure 1. The absorption spectra of the polymers in a) dilute CB solution and b) thin films; c) Gaussian peaks simulating absorption spectra of polymers in CB solution.

Table 1. Physical properties of PBDT-DTNT polymers.

Polymer	M_n/PDI [kDa][a)]	T_d [°C][b)]	λ_{max} [nm]			Film E_g [eV][c)]	IP [eV][d)]	EA [eV][e)]
			Solution	Film	Redshift			
PEH/dC10	34/1.87	450	598	650	52	1.65	5.32	3.67
PEH/dC6	33/1.61	458	618	651	32	1.63	5.29	3.66
PC6/dC10	23/1.56	458	636	706	70	1.58	5.17	3.59
PEH/BO	21/2.10	436	569	692	123	1.63	5.24	3.61
PC6/HD	20/1.98	425	584	648	64	1.60	5.22	3.62

[a)]Determined by GPC (150 °C trichlorobenzene) against PS standards; [b)]Thermal decomposition temperatures at 5% weight loss; [c)]Band gap calculated from the onset of the solid film absorption spectra; [d)]Measured by cyclic voltammetry; [e)]Determined from IP–E_g.

and an enhanced peak at ≈650 nm was observed. Weak shoulders at ≈700–720 nm for polymers in solution intensified into peaks. From solution to thin film, both intrachain conformation and interchain stacking are promoted and the random geometry, associated with high wavelength ICT absorption (around or below 600 nm), decreased. While the intermolecular stacking will usually lead to the lowest wavelength species (here should be 700–720 nm peaks), the peak at ≈650 nm can be attributed to a more planar geometry of the conjugated chain.

More detailed analysis of these absorption spectra was carried out by fitting the absorption profiles with Gaussians. Shown in Figure 1c is the peak analysis of the solution absorption spectra. For the first category of polymers with EH substitution on the NT units, the long alkyls (two C10 chains) on BDT units (PEH/dC10) retard intermolecular stacking. High density of the long alkyl chains increased the possibility of folded alkyl chains that suppressed the backbone interactions. While keeping the long alkyl chain on the BDT units and replacing the EH chain by C6 chain on the NT units (PC6/dC10), a significant absorption increase at 665 nm indicated enhanced chain planarity, which decreased steric hindrance of the BDT substitution and led to enhanced interchain π–π stacking. It should be noted that high density substitution on the BDT units, plus the branched substitution on NT units, caused PEH/dC10 and PEH/dC6 to exhibit the weakest absorption from 700 to 720 nm in the solid state. In the second category of polymers, monosubstitution on the BDT units led to low side chain density, which is favorable for the interdigitation of vertically adjacent chains; this can be seen from their strong absorption in 700–720 nm range.[34] However, a branched EH group on the NT units (PEH/BO) strongly reduced the interchain packing in solution and the ≈650 nm peak for this polymer was strongly reduced, which could be recovered from solution to solid transformation.

From the absorption onset, optical band gaps of the polymers were estimated to be 1.58–1.65 eV. A more detailed characterization of the energy levels was done using cyclic voltammetry (results summarized in Table 1 and voltammograms are shown in Figure S4 in the Supporting Information). The ionization potential (IP) values were estimated from the onset of the oxidation peaks as a function of saturated calomel electrode (SCE) in the voltammogram and calculated as IP = $e[E_{ox}–E_{ox}(Fc/Fc^+) + 4.80]$. It was reported that closer intermolecular packing would destabilize and raise the HOMO levels,[35,36] which is in good agreement with the measured energy levels of the polymers. PC6/dC10 with tight molecular packing gave a rather high-lying HOMO of –5.17 eV, whereas PEH/dC10 showed the lowest HOMO energy level at –5.29 eV. The approximate electron affinity (EA) values of these copolymers were in the range of 3.59–3.66 eV as estimated from the difference between the IP values and E_g^{opt}.[37]

2.3. Thin Film Morphology

The morphology of these polymers was studied using a range of characterization tools. In general, the crystalline information of these polymers and size scale of phase separation of their BHJ blends were taken into account. The film preparation followed the procedures of device fabrication, in which we saw that the additive, 1,8-diiooctane (DIO), had a profound effect on the morphology. Shown in **Figure 2** are the GIXD out-of-plane (OOP) linecut profiles of these polymer films and blend films processed under different conditions.[38] Diffraction patterns of pure polymers were shown in the Supporting Information. PEH/dC10 showed a π–π stacking reflection at 1.607 Å^{-1}, corresponding to a distance of 3.91 Å. The (100) lamellae stacking in the OOP direction is weak, since the crystal was face-on. The BHJ blend processed from CB showed similar GIXD results with an additional peak at 1.35 Å^{-1}, arising from PCBM. When processing the BHJ blends from CB/DIO, the (100) peak in OOP direction at 0.234 Å^{-1} (26.8 Å) was seen. The large interlamellae spacing was due to the long alkyl and thiophene side chains. Reducing the C10 alkyl chains to C6 (PEH/dC6) led to a drastic reduction in the (100) lamellae distance to 19.6 Å (0.321 Å^{-1}). By modifying the alkyl chains on the NT unit, more drastic changes were observed. While PC6/dC10 showed an obvious face-on orientation, adding PCBM into this polymer led to a strong edge-on orientation, strong (100) and (200) reflections were seen in the OOP profiles. When the blends were processed from CB, the (100) distance was calculated to be 26.7 Å, and after DIO was used, this value was increased slightly to 27.5 Å. The (100) peak intensity also increased when DIO was used and the crystal size grew from 103.6 Å to 178.6 Å, which translated to ≈3 more layers stacked together to form larger crystals. It is obvious that the additive increases the relative crystallinity of the polymer, which can be seen from the increased area of (100) peak. (Admittedly this is a rough estimation. A more accurate evaluation of the crystallinity requires recording the diffraction data over all reciprocal space, which requires rotations of the sample and detector to account for all directions of the scattering vector, and taking into account the

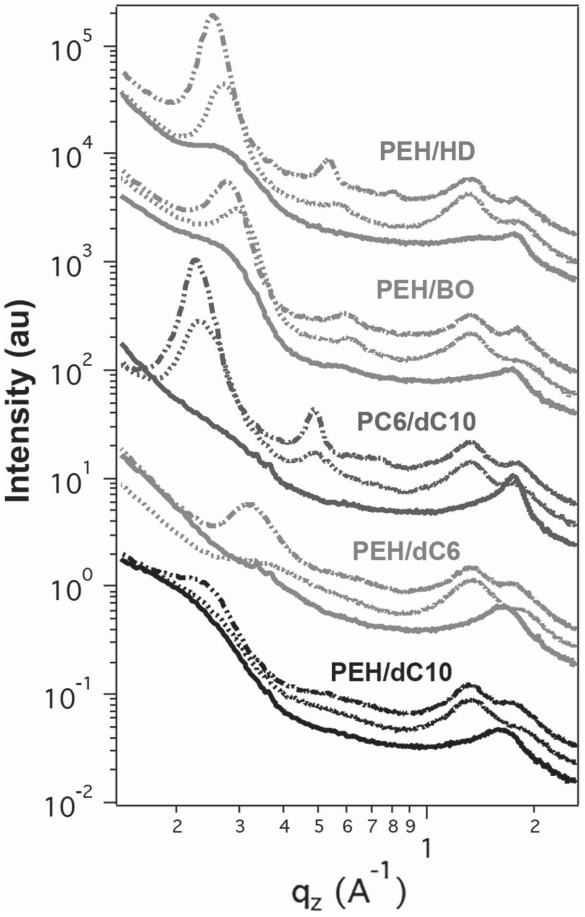

Figure 2. Out-of-plane linecut of GIXD results. Solid curve: pure polymer; dot curve: BHJ blends processed from CB; dash-dot curve: BHJ blends processed from CB/DIO.

incoherent scattering and the scattering from the amorphous materials.) DIO is essentially a long alkyl chain that can associate with the alkyl chains on the conjugated polymer. The vapor pressure of DIO is low, leading to a slower evaporation and a more stretched (zig-zag) conformation of the alkyl side chains and, therefore, a larger (100) distance.

The first category of polymers can be used to assess the relationship between the side chain structures and film properties. While it is obvious that different side chain length will affect the crystal spacing, a closer inspection reveals interesting information in the π–π stacking. For PEH/dC10, the π–π stacking distance is 3.91 Å, shorter side chain on the BDT units (PEH/dC6) slightly reduced this to 3.85 Å (1.632 $Å^{-1}$), but changing the branched EH side chain to linear C6 on the NT units reduced this value dramatically to 3.58 Å (1.756 $Å^{-1}$). Consequently, the presence of branched side chains strongly affected the interchain p-p stackings.

For the second category of polymers, similar trends in the (100) peak were observed. PEH/BO BHJ blends cast from CB showed a (100) peak at 0.297 $Å^{-1}$ (21.1 Å). With the use of DIO, this peak shifted to 0.278 $Å^{-1}$ (22.6 Å). The PC6/HD BHJ blends cast from CB showed a (100) peak at 0.272 $Å^{-1}$ (23.1 Å); and with the use of DIO, this peak shifted to 0.253 $Å^{-1}$ (24.8 Å). When comparing PEH/BO to PEH/dC10 or PEH/dC6 with more crowded side chains, a more pronounced (100) peak was seen for the PEH/BO BHJ blends, indicating that the replacement of double linear chains by branched chains could effectively reduce the side chain density, leading to strengthened lamellar packing. In the π–π stacking direction, the less substituted PEH/BO polymer showed a distance of 3.58 Å (1.753 $Å^{-1}$), which is nearly the same as that of PC6/dC10, confirming the previous argument. Replacing EH by C6 on the NT units, the PC6/HD showed a π–π stacking distance of 3.51 Å (1.787 $Å^{-1}$), which is the smallest for the materials under consideration in this study. The GIXD study clearly shows the importance of side chain engineering on the morphology of the thin films, the type of the side chain (linear or branched) affects more in the π–π stacking (010) direction, while the side chain density plays a significant role in the lamellar packing (100) direction. These properties will be translated to electronic properties and device performance, which will be analyzed in further discussions.

Phase separation of the BHJ blends was studied using RSoXS at carbon K-edge photon energy (284.2 eV), which yields the best contrast between fullerene and conjugated polymers.[38,39] Thin films processed from CB were investigated first with the results shown in **Figure 3**a. PEH/dC10 showed a broad peak at 0.018 $Å^{-1}$, corresponding to a center-to-center distance of 35 nm. The PEH/dC6 sample did not show an obvious peak over the scattering

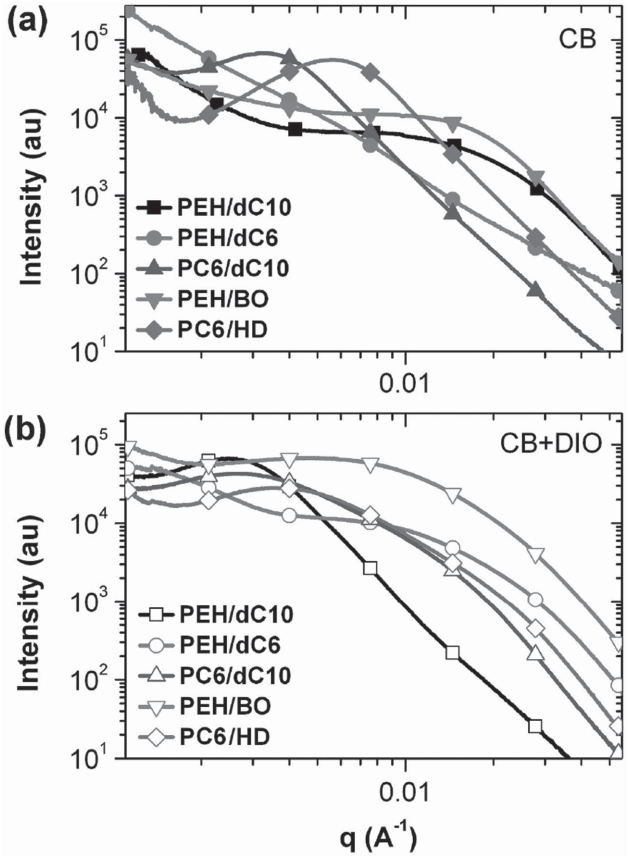

Figure 3. RSoXS profiles of a) CB and b) CB:DIO processed blend films at 284.2 eV photon energy. The scattering peaks correlated to the size of phase separation in BHJ thin films.

vector range investigated, indicating good mixing with PCBM. PC6/dC10 showed a strong scattering peak at 0.0034 $Å^{-1}$, corresponding to a distance of 185 nm. Such a large size scale most probably arose from PCBM aggregations. For the monosubstituted BDT-based polymers, PEH/BO showed a peak at 0.018 $Å^{-1}$, giving distance of 35 nm, and PC6/HD showed a peak at 0.0059 $Å^{-1}$, corresponding to a distance of 106 nm. Consequently, polymers with EH side chains on the NT units suppress large scale phase separation with PCBM, giving rise to a more homogeneous mixture. When thin films were processed from CB and DIO (Figure 3b), PEH/dC10 developed a large size scale phase separated morphology with a peak observed at 0.0026 $Å^{-1}$, corresponding to a distance of 245 nm. PEH/dC6, which did not show phase separation, developed a broad hump from 0.01 to 0.03 $Å^{-1}$. PC6/dC10 showed a peak at 0.0028 $Å^{-1}$ and a hump at 0.017 $Å^{-1}$, characteristic of a multilength scale morphology. The BDT monosubstituted analogue PC6/HD showed a similar morphology, with a reflection characteristic of a large scale at 0.004 $Å^{-1}$ and a small scale hump at 0.02 $Å^{-1}$. The PEH/BO polymer showed a broad distribution from 0.004 to 0.03 $Å^{-1}$. In comparison, we noticed that EH substitutions on the NT units were more likely to develop broad range of phase separated structures, while polymers with C6 substituted on the NT units would show multilength scale morphology. These results are in good agreement with the AFM images shown in the Supporting Information, and the length scale of phase separation is an important parameter that governs the device performances, which will be discussed in the next section.

2.4. Photovoltaic Properties

The photovoltaic properties of the resulting polymers as electron donors were investigated with an inverted device structure by using our newly developed poly[(9,9-bis(3-(*N*,*N*-dimethylamino)propyl)-2,7-fluorene)-alt-2,7-(9,9-bis(3-ethyl(oxetane-3-ethyloxy)hexyl)fluorene)] (PF_3N-OX) as the cathode buffer layer. The interfacial layer of cross-linked PF_3N-OX could effectively modify the electronic properties of ITO and improve electron extraction properties with the additional benefit of enhanced device stability.[40–44] MoO_3/Al was used as the anode for the inverted cells. CB was used as the major solvent and 2 vol% of DIO was used as processing additive to optimize the morphology (polymer:$PC_{71}BM$ = 1:1 w/w after optimization).

The current density–voltage (*J*–*V*) curves of the devices were shown in **Figure 4**a,b and **Table 2**, and the hole mobility (μ_h) of the blends was examined by the space charge limited current (SCLC) method in single carrier devices. We have also carried out device fabrication using 1,2-dichlorobenzene (DCB) as the processing solvent and the results are summarized in Table S1 in the Supporting Information. The devices prepared from CB solvent system showed an overall superior performance to devices prepared from the DCB solvent system and are, therefore, discussed in detail. For the first category of polymers, PEH/dC10 and PCBM blends processed from CB gave a low current of 6.3 mA cm^{-2} with PCE of 2.46%. We see a 35 nm size scale of phase separation for this device, which is suitable for the generation of a high current. However, the low crystallinity, as seen by GIXD, prohibited the charge transport and energy harvesting. A quite low hole mobility is also observed. Adding 2 vol% DIO leads to a further decrease in both the current and PCE, as a result of the enlarged phase separation observed by RSoXS. Reducing the substituted chain length on BDT to C6 (PEH/dC6) leads to a better mixing with PCBM. A low current of 8.67 mA cm^{-2} with PCE of 3.15% is observed and a low fill factor (FF) of 38% is seen, as a result of mixing. Adding DIO leads to a drastic increase in device performance. The current increased to 15.57 mA cm^{-2} and PCE increased to 7.88%. The broad phase separation (60–20 nm, 0.01–0.03 $Å^{-1}$) on a smaller size scale is critical for enhancing device performance, plus enhanced crystallinity leads to a much higher hole mobility. For PC6/dC10, CB-cast thin films showed a moderate PCE of 6.10% with a 185 nm size scale of phase separation. It is quite unexpected that high PCE could be obtained with such a large length scale phase separation and thus we suspect that the mixing region in this case provides a good carrier yield. A very high mobility was seen in this case. When DIO was added, the multilength scale morphology with increased crystallinity elevates the PCE to 6.89%. For the second category of polymers, CB and CB with DIO processing show similar device performance. We have shown previously that PEH/BO yielded a 35 nm length scale for phase separation with CB processing and a quite broad phase separation (157–20 nm, 0.004–0.03 $Å^{-1}$) for processing from CB and DIO. The presence of a small size scale phase separation in both cases is the key in delivering a high current. The PC6/HD polymer showed a PCE of 6.12% in CB+DIO processed device.

Figures 4c and 1d showed the external quantum efficiency (EQE) curves of the polymer:$PC_{71}BM$ blends, the J_{sc} calculated from the integrated value of the EQE spectrum was in good agreement with the device results. For CB processed thin films, PC6/dC10 showed the best EQE over a broad wavelength range. Together with other device parameters and SCLC mobility, we saw this material had a superior nanostructure. Enhanced crystallinity with a larger size scale of phase separation yielded quite good performance. It should be noted that the all linear alkyl design for this polymer and the induced strong π–π stacking lead to a high HOMO energy level. Thus, in devices, only a 0.74 V V_{oc} was seen, prohibiting further enhancement of efficiency. PEH/BO showed the best EQE response in the second category of materials. The high EQE value in the 650–750 nm region was unique and indicated good light harvesting from the polymer, which benefitted from a well-defined small length scale of phase separation. For films processed from CB and DIO, a drastic improvement in EQE was seen for PEH/dC6. Both intensity and wavelength regions were improved. The 600–750 nm wavelength region developed into a broad peak. The broad but small length scale phase separation plus enhanced structural ordering of polymer gave rise to better light harvesting of both polymer and PCBM. The branched EH substitution on NT unit blocked close π–π stacking, and thus in devices a good V_{oc} of 0.8 V was obtained.

These device results, together with structural characterization, provide designing protocols for developing good performing polymers of this kind and several key principles can be summarized as follows. (1) The side chain density will affect the structure order of the resulting polymers especially in the lamellar packing direction; low side chain density will facilitate

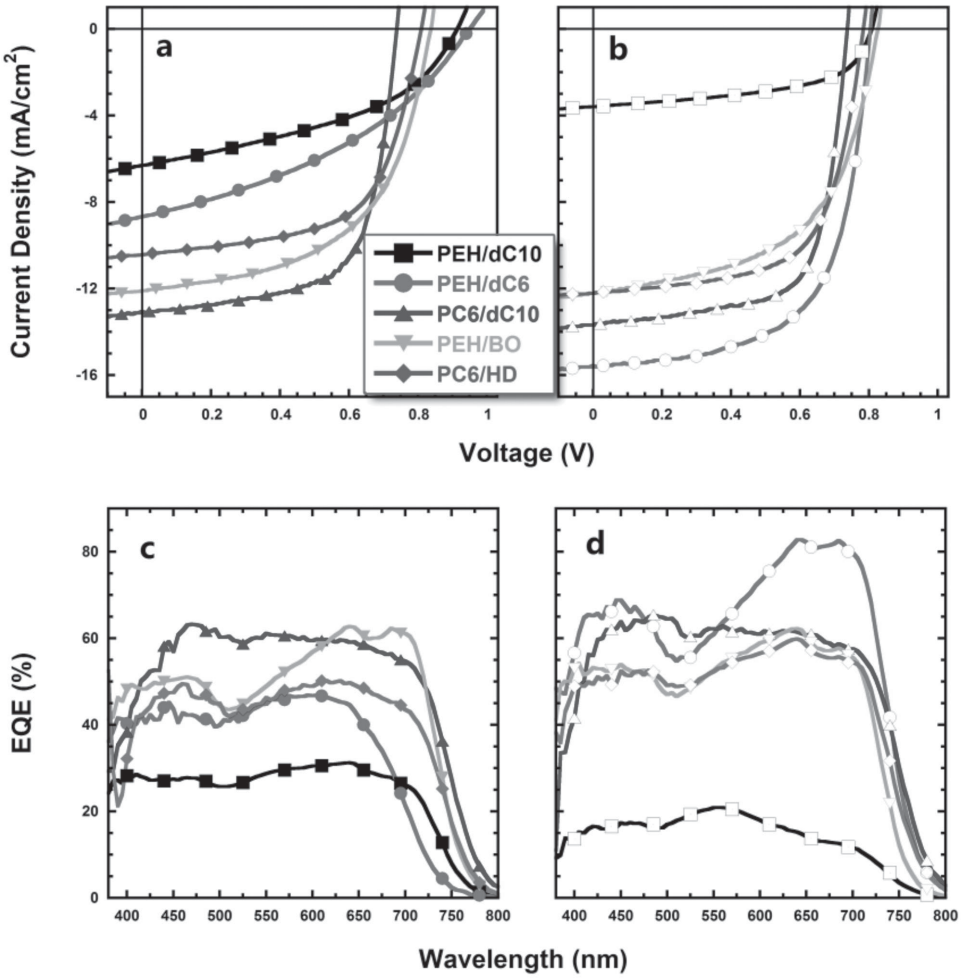

Figure 4. Current–voltage characteristics of PSCs for each polymer processed from a) CB and b) CB:DIO, under simulated AM 1.5G illumination (100 mW cm^{-2}); external quantum efficiency curves of the devices for each polymer processed from c) CB and d) CB:DIO.

the vertical interdigitation of adjacent chains. (2) The change of side chain type from branched to linear substitution will lead to enhanced cofacial π–π stacking of conjugated polymer chains, which is helpful to promote structure order but detrimental for the energy level. (3) A broad size scale of phase separation or multilength scale morphology covering the exciton diffusion length will be beneficial to generate a higher current. Combining these observations, we would argue that designing materials using mixed linear and branched side chains at the shortest length to provide enough solubility will be of high possibility to obtain high performing photon-active polymers.

Table 2. Photovoltaic performances of devices with PBDTDTNT:$PC_{71}BM$ (weight ratio of 1:1) under the illumination of AM 1.5G, 100 mW cm^{-2}.

Polymer[a)]	DIO	J_{sc} [mA cm^{-2}]	V_{oc} [V]	FF [%]	PCE (Avg.) [%]	Mobility [cm^2 V^{-1} s^{-1}]
PEH/dC10	–	6.30	0.91	43	2.46(2.21)	1.89×10^{-5}
	2%[b)]	3.59	0.81	54	1.59(1.42)	1.51×10^{-5}
PEH/dC6	–	8.67	0.95	38	3.15(2.95)	4.23×10^{-5}
	2%[b)]	15.57	0.80	63	7.88(7.62)	1.43×10^{-4}
PC6/dC10	–	13.05	0.74	63	6.10(5.95)	9.95×10^{-5}
	2%[b)]	13.67	0.74	68	6.89(6.55)	1.25×10^{-4}
PEH/BO	–	12.10	0.84	55	5.57(5.31)	4.79×10^{-5}
	2%[b)]	12.22	0.83	55	5.60(5.40)	5.45×10^{-5}
PC6/HD	–	10.44	0.81	61	5.17(5.07)	6.22×10^{-5}
	2%[b)]	12.22	0.78	64	6.12(5.93)	7.45×10^{-5}

[a)]The average values were calculated over eight devices; [b)]Devices prepared from blends solution in CB containing 2% (v/v) of the processing additive DIO.

2.5. Optimization of the Active Layer Thickness

All the reported NT-based polymers exhibited excellent PSC performance with thick BHJ composite layer due to their high hole mobility,[29,31] which decreases the probability of charge-carrier recombination and increases the number of photons absorbed.[45–47] Recently Yan et al. reported a series of high-performance polymers for thick-film PSCs, the branching position and size of the alkyl side chains are of critical importance in enabling a well-controllable aggregation of polymers, which played an important role in maintaining high mobility

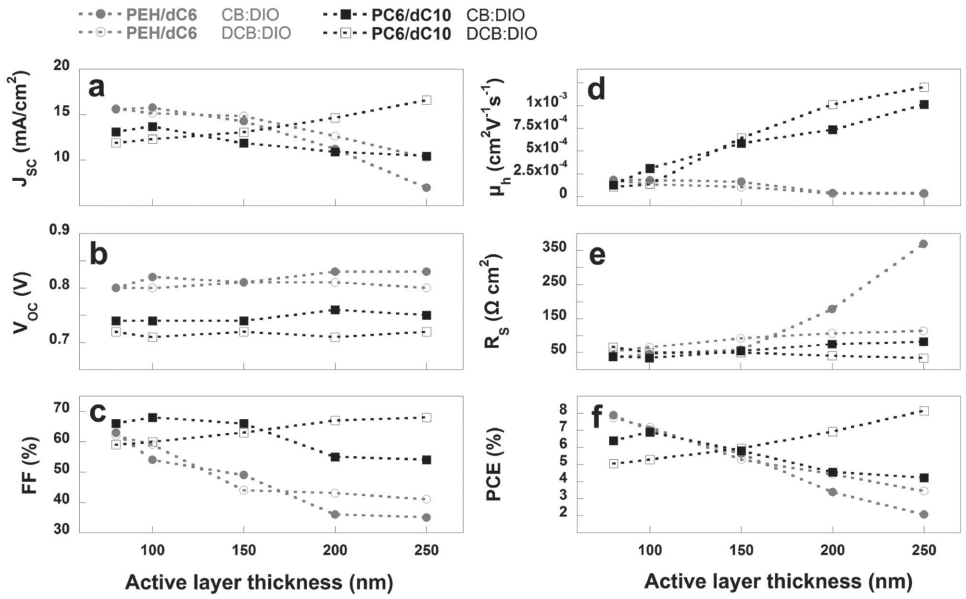

Figure 5. Device performance of the inverted PSCs based on PEH/dC6 and PC6/dC10 with different BHJ thickness: a) J_{sc}, b) V_{oc}, c) FF, d) μ_h, e) R_S, and f) PCE.

and FF in thick BHJ devices.[48] Herein using a PSC geometry, the influence of the thickness of the BHJ composite active layer was investigated. The two polymers with the highest hole mobility and PSC performance (PEH/dC6 and PC6/dC10) were chosen for this study. The active layer thickness was varied by changing the concentration of the blend solution and the spin-coating speed. Active layers were prepared from CB and DCB solutions with 2 vol% DIO. **Figure 5** shows the variation of J_{sc}, V_{oc}, FF, μ_h, series resistance (R_S) and PCE of the PSC devices based on the two polymers with increasing active layer thickness. Detailed data are given in Tables S2 and S3 in the Supporting Information.

For PEH/dC6:PCBM films prepared from CB:DIO and DCB:DIO, J_{sc} and FF decreased when the film thickness increased. Hole mobilities decreased slightly with increasing thickness. V_{oc} remained constant for all the thicknesses. PEH/dC6 showed a rapid increase in series resistance with increasing thickness and, thus, the PCE of the devices decreased markedly, from ≈8% to 2% when the thickness increased from 80 to 250 nm. PC6/dC10 polymer showed a more complicated response to changes in the thickness. When processed from CB/DIO, J_{sc} decreased with increasing film thickness, whereas devices processed from DCB/DIO showed a completely different trend. CB/DIO processed devices showed a slightly larger V_{oc} compared to DCB/DIO processed devices, both remained relatively constant with different thicknesses. The FF of CB/DIO processed devices remained relatively constant for thicknesses <150 nm and then decreased rapidly with increasing thickness. DCB/DIO processing led to a continuous increase in FF. Together, these translated to a decreasing PCE in CB/DIO processed devices (from 6.39% to 4.22%) and increasing PCE in DCB/DIO processed devices (from 5% to 8.14%). Remarkably, at an active layer thickness of 250 nm, a PCE of 8.14% was obtained higher than any other devices in this study. Another unique feature of PC6/dC10 was that the hole mobility increases with the increase in the film thickness. It was particularly important to achieve a high performance with the thicker active layers. In fact, even for CB/DIO processed thin film, the efficiency drop was the lowest in this study when the active layer thickness was increased. Consequently, thickness control proved to be another parameter that needs to be considered in device optimization. Thus, chemical structure, processing conditions, morphology, and thickness form a quite intricate matrix that determines the final performance of PSC devices.

Thickness-change-related device performances are more of the device engineering issue, where the recombination of the photon-generated charge carrier is the key.[47] The decreasing mobility of PEH/dC6 polymer under both processing conditions correlates well with the device performance decrease. For PC6/dC10, different processing conditions led to completely opposite trends in solar cell performance. Consequently, structural characterization was performed to provide some insight. Both GIXD and RSoXS were performed on active layers with thickness of 80, 150, 200, and 250 nm (**Figure 6**). PC6/dC10 showed a highly ordered edge-on structure with four orders of the (100) reflection being observed in the OOP direction. Complementary π–π stacking in the in-plane direction was observed. The reflections from the (100) planes, (010) planes, and PCBM were analyzed and the results are summarized in Figure 6b. The coherence length or size of the crystal in the (100) direction for films cast from CB/DIO processing did not show obvious trend, whereas for films cast from DCB/DIO a continuous increase was observed with increasing film thickness. A more obvious increase in crystal size in the (010) direction was seen in the DCB/DIO processed films, from 37 Å in the 80 nm film to 42 Å in the 250 nm film, whereas this remained constant at 40–42 Å for the CB/DIO processed films. The size of the PCBM aggregates showed a similar trend and size scales for both DCB/DIO and CB/DIO processing. These results showed quite interesting properties of PC6/dC10. The 2D GIXD patterns

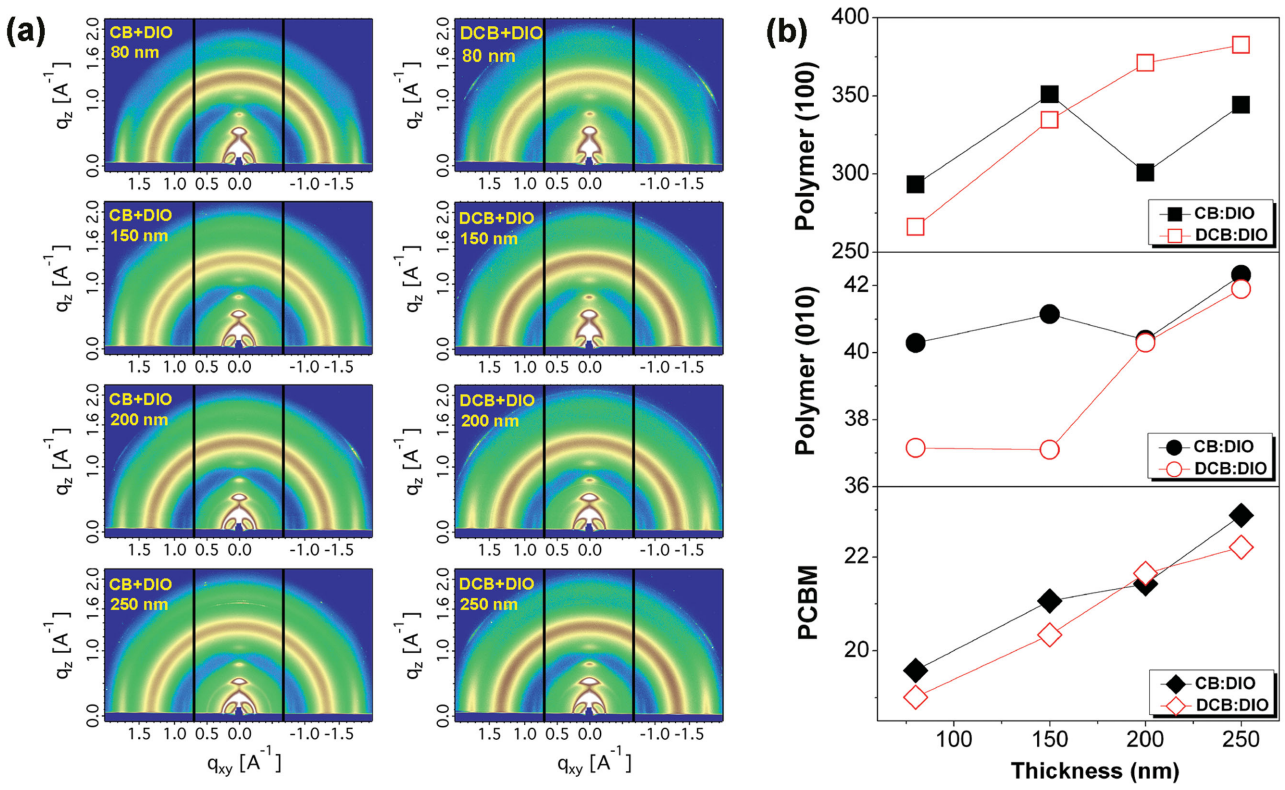

Figure 6. A) GIXD diffractograms and b) peak analysis coherence length of polymer and PCBM in PC6/dC10:PCBM blended films with different thickness. The unit of crystal size is Å.

were essentially the same for the 80 and 250 nm thick films, indicating that the polymer assumes an edge-on orientation regardless of film thickness under the same processing conditions. The increase of crystal size in both the (100) and (010) directions reflects an improved crystal quality within the film, which, we feel, leads to a domain connectivity throughout the film to serve as relay centers to connect long polymer tie chains, which help maintain a high FF and mobility in thicker devices.

RSoXS (**Figure 7**) of the CB/DIO processed thin film, shows a slightly reduced length scales of phase separation in thin film (80 nm) comparing to 250 nm thicker film, corresponding to a slightly larger current measured. When the film became thicker, the scattering signal became weaker. DCB/DIO processed thick film showed a more distinguished phase separation peak. These results indicate that the DCB/DIO processing led to a better defined phase-separated morphology with stronger compositional variations in thicker films, which helps to increase the current and FF in thicker films and, thus, enhanced performances in thicker films were observed.

3. Conclusion

In conclusion, we have demonstrated that systematic tuning of side chains in conjugated polymers can be an effective method to fine tune both the electronic structure and film morphology, which provides new handles to optimize the performance of plastic solar cells. It is shown that chain aggregation and crystallization, both in solution and thin films, are strongly affected by the choice of side chain substituent, where the type and density of side chains are critical. For the side chain type, compared with branched alkyl chains, linear side chains would facilitate the π–π stacking and make it more compact for charge transfer. For side chain density, proper use of branched side chains instead of double linear chains could significantly reduce the side chain density, which is favorable for lamellar packing while ensuring comparable solubility. Polymers with different side chains behave differently under different processing conditions, thus the optimization matrix is enlarged. We also demonstrated that solar cell device performances also depend on film thickness over a broad range, indicating thicker devices should be investigated for newly developed polymers. A structure–property relationship regarding film thickness and performance is also shown.

4. Experimental Section

Measurements: The ^{13}C NMR of compound **7a** was measured on a Bruker AVANCE Digital 400 MHz NMR workstation. The remaining ^{13}C NMR and ^{1}H NMR data were collected on a Bruker AVANCE Digital NMR workstation operating at 300 MHz, respectively. Chemical shifts were reported as δ value (ppm) relative to an internal tetramethylsilane standard. Molecular weights of the polymers were determined using an Agilent Technologies PL-GPC 220 high-temperature chromatograph in 150 °C 1,2,4-trichlorobenzene using a calibration curve of polystyrene standards. Mass spectrometry (MS) data were obtained on a WatersTQD with atmospheric pressure chemical ionization (APCI) resource. UV–vis absorption spectra were measured using a SHIMADZU UV-3600 spectrophotometer. TGA measurements were

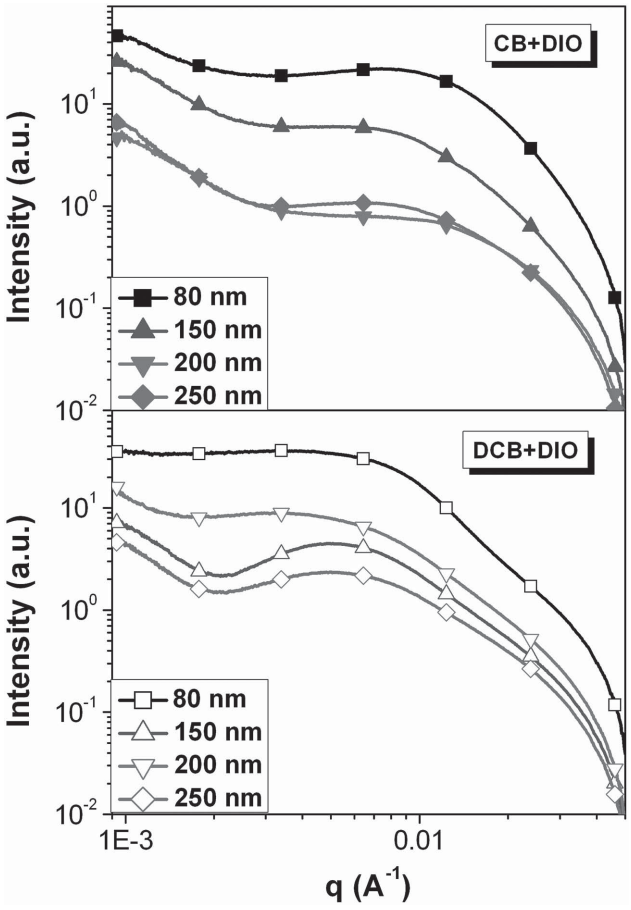

Figure 7. RSoXS profiles of PC6/dC10:PCBM films with different thickness processed from a) CB:DIO and b) DCB:DIO.

performed on a Netzsch TG 209 in nitrogen, with a heating rate of 20 °C min^{-1}. DSC measurements were performed on a Netzsch DSC 204. EQE measurements were taken using a monochromator (Newport, Cornerstone 130) joined to the same xenon lamp and a lockin amplifier (Stanford Research Systems, SR 830) coupled to a light chopper. AFM measurements were performed on a Digital Instrumental DI multimode nanoscope IIIa in tapping mode. The electrochemical cyclic voltammetry experiments were conducted on a CHI800 electrochemical workstation equipped with a graphite electrode coated with thin copolymer film as the working electrode, an SCE as the reference electrode, and a Pt sheet counter electrode in a 0.1 M tetrabutylammoniumhexafluorophosphate (Bu_4NPF_6) acetonitrile solution, at a scan rate of 50 mV s^{-1} at room temperature. The potential of the saturated calomel reference electrode was internally calibrated using the ferrocene/ferrocenium redox couple (Fc/Fc^+), which has a known reduction potential of −4.8 eV. Thus, the IP values of the copolymers were calculated according to the following empirical formulas

$$IP = e[E_{ox} - E_{ox}(Fc/Fc^+) + 4.80](eV)^{[49]} \quad (1)$$

The E_{ox} is the onset oxidation potential versus SCE. It should be pointed out that the reductive curves of the copolymers could hardly be obtained. Therefore, the EA values of the copolymers were estimated from their optical band gaps and IP values using the equation of

$$EA = IP - E_g^{opt} \quad (2)$$

where E_g^{opt} denotes the optical band gaps of the copolymers and EA calculated here from the E_g^{opt} was approximate values since it ignores the exciton binding energy.[37]

Characterization of PSCs: PCEs were measured under a computer-controlled Keithley 2400 sourcemeter under 1 sun, AM 1.5G solar simulator (Japan, SAN-EI, XES-40S1). The light intensity of the sun simulation was calibrated by a standard silicon solar cell (certified by NREL) before the testing, giving a value of 100 mW cm^{-2} during the test. The current density–voltage (*J–V*) characteristics of hole-only devices were recorded with a Keithley 236 sourcemeter under dark. The EQE spectra were performed on a commercial EQE measurement system (Beijing, Zolix, DSR 100UV-B).

Inverted PSC Fabrication: The ITO-coated glass substrates were cleaned by sonication in acetone, detergent, deionized water, and isopropyl alcohol, and dried in oven at 80 °C for 12 h before used. Then the ITO substrates were transferred into an N_2 protected glove box where the H_2O concentration is ≤0.5 ppm and O_2 concentration is ≤20 ppm. The cross-linkable polymer PF_3N-OX (0.5 mg mL^{-1}) was spin-casted from its methanol:acetic acid (99:1 v/v) solution onto the precleaned ITO substrates to form ≈5 nm thin film, and the cross-linking process was carried out by heating the half-dried films under 150 °C and fluorescence lamp illumination (no UV lamps required) for 20 min. The active layer solutions were prepared by dissolving polymer:$PC_{71}BM$ (1:1, w:w) blend into chlorobenzene:1,8-diiodoctane (98:2 v/v) or dichlorobenzene:1,8-diiodoctane (98:2 v/v) with polymer concentration at 10 mg mL^{-1}. These solutions were heated at 60 °C overnight to completely dissolve the polymer and fullerene. After cooling down to RT and without any filtering, the active layer solutions were spin-coated onto PF_3N-OX to yield 90 ± 10 nm thick active layers by adjusting the spin-coating speed. After that, about 10 nm molybdenum oxide (MoO_3) and 100 nm aluminum were thermally deposited on top of the active layer through a shadow mask in a vacuum chamber with base pressure of 2×10^{-6} mbar. The effective area of a device was defined to be 0.16 cm^2 by the shadow mask.

Hole Mobility Measurement: Hole-only devices were fabricated with the device structure ITO/PEDOT:PSS(45 nm)/polymer:$PC_{71}BM$(90 nm)/MoO_3(10 nm)/Al. The mobility was determined by fitting the dark current to the model of single carrier SCLC, which is described by the equation

$$J = \frac{9}{8}\varepsilon_0\varepsilon_r\mu_h\frac{V^2}{d^3} \quad (3)$$

where J is the current, μ_h is the zero-filed mobility, and ε_0 and ε_r are the permittivity of free space and relative permittivity of the material, respectively. d is the thickness of the organic layer, and V is the effective voltage. The effective voltage can be obtained by subtracting the built-in voltage (V_{bi}) and the voltage drop (V_s) from the substrate's series resistance from the applied voltage (V_{appl}), $V = V_{appl} - V_{bi} - V_s$. The hole mobility can be calculated from the slope of the $J^{1/2}$–V curves.

GIXD Characterization: Grazing incidence X-ray scattering characterization of the thin films was performed at the Advanced Light Source on beamline 7.3.3, Lawrence Berkeley National Lab (LBNL). The scattering signal was recorded on a 2D detector (Pilatus 3M) with a pixel size of 0.172 mm by 0.172 mm. The samples were ≈15 mm long in the direction of the beam path, and the detector was located at a distance of ≈300 mm from the sample center (distance calibrated using a silver behenate standard). The incidence angle of 0.16° was chosen which gave the optimized signal-to-background ratio. The beam energy was 10 keV, operating at top-off mode. Typically, 30 s exposure time was used to collect diffraction signals. All GIXD experiments were done in helium atmosphere. The data was processed and analyzed using Nika software package.

RSoXS Characterization: RSoXS was performed at beamline 11.0.1.2 Advanced Light Source, LBNL. Thin film samples were spin-casted on to PF_3N-OX covered SiO_2 wafers. This film preparation process is the same with device fabrication. Then dilute HF solution was used to float the BHJ layer, which was then transferred onto Si_3N_4 substrate (Norcada Inc.) and experiment was done in transition mode. The scattering signals were collected in vacuum using Princeton Instrument PI-MTE CCD camera.

Materials Preparation: 3-Hexylthiophene and 3-decylthiophene were purchased from Accela ChemBio Co. 2-Butyl-1-octanol and

2-hexyl-1-decanol were purchased from Sigma-Aldrich. All of these chemicals were used as received. 4,8-dehydrobenzo[l,2-b:4,5-b′] dithiophene-4,8-dione,[50] tributyl-(4-hexyl-2-thienyl)stannane, tributyl-[4-(2-ethylhexyl)-2-thienyl] stannane,[51] monomer **4a** and **4b**[52] were synthesized according to the reported methods. The starting compound NT was synthesized using the method reported by Mataka et al.[53] Tetrahydrofuran (THF) was dried over Na/benzophenone ketyl and freshly distilled prior to use. Detailed synthesis and characterization of intermediates were summarized in the Supporting Information. The key monomers and polymer syntheses were listed below:

4,8-di(2,3-Dialkylthiophen-5-yl)-benzo[1,2-b:4,5-b′]dithiophene(2), compound **1** (45 mmol, 1a/1b), was dissolved in anhydrous THF (40 mL) in a three-neck flask under an argon atmosphere. The solution was cooled to 0 °C, and a solution of n-BuLi (1.6 M in hexane, 31 mL, 49.5 mmol) was added dropwise with stirring. The reaction mixture was then heated to 50 °C for 2 h. Subsequently, 4,8-dehydrobenzo[l,2-b:4,5-b′]dithiophene-4,8-dione (3.3 g, 15 mmol) was quickly added, and the reaction mixture was stirred at 50 °C for 1 h. Then the reaction mixture was cooled to ambient temperature. A solution of $SnCl_2{\cdot}2H_2O$ (27.1 g, 120 mmol) in 10% HCl (48 mL) was then added. The reaction mixture was stirred for an additional 1.5 h and poured into ice water. The mixture was extracted twice with petroleum ether. The organic phase was dried over anhydrous $MgSO_4$ and concentrated. The crude product was purified by silica-gel chromatography using petroleum ether as the eluent to yield the pure product.

4,8-di(2,3-Dihexylthiophen-5-yl)-benzo[1,2-b:4,5-b′]dithiophene (**2a**) was obtained as yellow solid (6.7 g, yield 65%). ^{1}H NMR ($CDCl_3$, 300 MHz), δ (ppm): δ7.70 (d, 2H), 7.45 (d, 2H), 7.22 (s, 2H), 2.82 (t, 4H), 2.61 (t, 4H), 1.79–1.60 (m, 8H), 1.50–1.26 (m, 24H), 0.91 (m, 12H). ^{13}C NMR ($CDCl_3$, 75 MHz), δ (ppm): δ140.19, 138.86, 138.12, 136.37, 135.10, 129.86, 127.28, 124.15, 123.58, 31.84, 31.82, 31.67, 30.83, 29.22, 29.17, 28.35, 28.05, 22.71, 22.65, 14.15, 14.13. MS (APCI, m/z): calcd. for $C_{42}H_{58}S_4$ $[M+1]^+$, 691.3; found, 691.5.

4,8-di(2,3-Didecylthiophen-5-yl)-benzo[1,2-b:4,5-b′]dithiophene (**2b**) was obtained as yellow viscous solid (6.4 g, yield 47%). ^{1}H NMR ($CDCl_3$, 300 MHz), δ (ppm): δ7.68 (d, 2H), 7.43 (d, 2H), 7.21 (s, 2H), 2.81 (t, 4H), 2.60 (t, 4H), 1.62–1.75 (m, 8H), 1.28 (m, 56H), 0.88 (m, 12H).^{13}C NMR ($CDCl_3$, 75 MHz), δ (ppm): δ140.17, 138.86, 138.09, 136.36, 135.08, 129.84, 127.22, 124.14, 123.56, 31.91, 31.82, 30.79, 29.65, 29.63, 29.61, 29.55, 29.49, 29.43, 29.34, 28.31, 28.00, 22.67, 14.07.MS (APCI, m/z): calcd. for $C_{58}H_{90}S_4$ $[M+1]^+$, 915.6; found, 915.5.

4,8-di[2-(2′-Butyl-1′-octyl)thiophen-5-yl]-benzo[1,2-b:4,5-b′]dithiophene (**5a**) was synthesized according to the similar procedure for 2 h. Yellow viscous oil (7.25 g, yield 70%).^{1}H NMR ($CDCl_3$, 300 MHz), δ (ppm): δ7.62 (d, 2H), 7.43 (d, 2H), 7.28 (d, 2H), 6.87 (d, 2H), 2.84 (d, 4H), 1.78–1.65 (m, 2H), 1.45–1.20 (m, 32H), 0.88 (t, 12H).^{13}C NMR ($CDCl_3$, 75 MHz), δ (ppm): δ145.74, 139.05, 137.25, 136.55, 127.72, 127.45, 125.40, 124.13, 123.43, 40.07, 34.73, 33.43, 33.11, 31.94, 29.71, 28.96, 26.69, 23.07, 22.74, 14.19.MS (APCI, m/z): calcd. for $C_{42}H_{58}S_4$ $[M+1]^+$, 691.3; found, 691.6.

4,8-di[2-(2′-Hexyl-1′-decyl)thiophen-5-yl]-benzo[1,2-b:4,5-b′]-dithiophene (**5b**) was synthesized according to the similar procedure for 2h. Yellow viscous oil (8.67 g, yield 72%).^{1}H NMR ($CDCl_3$, 300 MHz), δ (ppm): δ7.64 (d, 2H), 7.44 (d, 2H), 7.29 (d, 2H), 6.88 (d, 2H), 2.85 (d, 4H), 1.75 (m, 2H), 1.60–1.10 (m, 48H), 0.90 (t, 12H).^{13}C NMR ($CDCl_3$, 75 MHz), δ (ppm): δ145.75, 139.05, 137.24, 136.55, 127.71, 127.42, 125.37, 124.13, 123.42, 40.08, 34.74, 33.43, 31.94, 30.03, 29.68, 29.62, 29.38, 26.68, 22.72, 14.14.MS (APCI, m/z): calcd. for $C_{50}H_{74}S_4$ $[M+1]^+$, 803.5; found, 803.5.

3,7-di(3-Hexylthiophen-5-yl)-naphtho[1,2-c:5,6-c]bis[1,2,5]thiadiazole (**7a**): Naphtho[1,2-c:5,6-c]bis[1,2,5]thiadiazole (0.49 g, 2 mmol) was dissolved in 10 mL vitriol oil and heated to 60 °C. Then *N*-bromosuccinimide (0.78 g, 4.4 mmol) was added in three portions over the course of 2 h. Subsequently, the reaction mixture was stirred for 24 h. Then the reaction mixture was poured into water, and the crude product was precipitated and collected by filtration. The residue was washed with water, ethanol, and THF. Without further purification, the bromide product was dried in the vacuum drying oven for use because it did not readily dissolve in common solvents. The bromide product and tributyl-(4-hexyl-2-thienyl)-stannane (2 g, 4.4 mmol) was added to 30 mL of dry DMF in a flask. The reaction mixture was purged with argon for 15 min. Then, the catalyst $Pd(PPh_3)_4$ (30 mg, 1.5%) was added and the solution was purged with argon for an additional 15 min. The reaction mixture was heated to 120 °C with stirring for 8 h. Then the reaction mixture was cooled to ambient temperature and poured into methanol to precipitate the crude product. After filtration, the residue was then purified by chromatography using a mixture of petroleum ether and CH_2Cl_2 as the gradient eluent. Finally the product was obtained as a salmon pink solid (0.38 g, yield 33%). ^{1}H NMR ($CDCl_3$, 300 MHz), δ (ppm): δ9.02 (s, 2H), 8.14 (s, 2H), 7.13 (s, 2H), 2.73 (t, 4H), 1.73 (m, 4H), 1.25–1.57 (m, 12H), 0.92 (t, 6H).^{13}C NMR ($CDCl_3$, 400 MHz), δ (ppm): δ153.06, 152.06, 143.96, 138.16, 129.34, 126.34, 124.34, 122.00, 121.86, 31.20, 30.16, 29.99, 28.55, 22.12, 13.57. MS (APCI, m/z): calcd. for $C_{30}H_{32}N_4S_4$ $[M+1]^+$, 577.1; found, 577.5.

3,7-di[3-(2′-Ethyl-1′-hexyl)thiophen-5-yl]-naphtho[1,2-c:5,6-c]bis[1,2,5]-thiadiazole (**7b**) was synthesized according to the similar procedure for **7a** assalmon pink solid (0.57 g, yield 45%). ^{1}H NMR ($CDCl_3$, 300 MHz), δ (ppm): δ8.74 (s, 2H), 8.01 (s, 2H), 7.07 (s, 2H), 2.65 (d, 4H), 1.70 (m, 2H), 1.50–1.20 (m, 16H), 0.95 (t, 12H).^{13}C NMR ($CDCl_3$, 75 MHz), δ (ppm): δ153.24, 152.22, 143.12, 138.39, 130.24, 126.47, 124.46, 123.39, 121.85, 40.40, 34.78, 32.59, 28.97, 25.72, 23.16, 14.22, 10.92. MS (APCI, m/z): calcd. for $C_{34}H_{40}N_4S_4$ $[M+1]^+$, 633.2; found, 633.7.

Synthesis of polymer PEH/dC6: The comonomer 8b (0.25 mmol) and 3a (0.25 mmol) were mixed in 5 mL of toluene and 0.5 mL of DMF. After being purged with argon for 15 min, $[Pd(PPh_3)_4]$ (10 mg) was added as the catalyst, and the mixture was then purged with argon for 5 min. The reaction mixture was stirred and heated to reflux for 42 h. Then 2-(tributylstannyl)thiophene and 2-bromothiophene were added to end cap the polymer chain. The reaction mixture was cooled to room temperature and dropped into methanol. The polymer was precipitated and then collected by filtration. The polymer was subjected to Soxhlet extraction with methanol, acetone, and dichloromethane. The solid was dried under vacuum. After drying in the vacuum drying oven, the polymer was dissolved in toluene, then the Pd-thiol gel (Silicycle Inc.) (30 mg) was added and the solution was stirred for 2 h followed by silica-gel chromatography with toluene eluent. The polymer was reprecipitated using methanol and dried. Finally, PEH/dC6 was obtained as dark purple solid.

PEH/dC10, PEH/BO, PC6/HD, and PC6/dC10 were synthesized according to the similar procedures for P2EH/dC6 from corresponding monomers. PEH/BO: Yield (76%). GPC: M_n = 21 kDa, M_w = 45 kDa, PDI = 2.10. T_d = 436 °C.

PEH/dC6: Yield (83%). GPC: M_n = 33 kDa, M_w = 53 kDa, PDI = 1.61. T_d = 458 °C.

PC6/HD: Yield (70%). GPC: M_n = 20 kDa, M_w = 39 kDa, PDI = 1.98. T_d = 425 °C.

PC6/dC10: Yield (72%). GPC: M_n = 23 kDa, M_w = 36 kDa, PDI = 1.56. T_d = 458 °C.

PEH/dC10: Yield (83%). GPC: M_n = 34 kDa, M_w = 64 kDa, PDI = 1.87. T_d = 450 °C.

Supporting Information

Supporting Information is available from the Wiley Online Library or from the author.

Acknowledgements

The authors thank the financial support from the Ministry of Science and Technology (No. 2014CB643501), the Natural Science Foundation of China (Grant Nos. 21125419, 51361165301 and 21490573), and the Guangdong Natural Science Foundation (Grant No. S2012030006232). Portions of this research were carried out at beamline 7.3.3 and 11.0.1.2

at the Advanced Light Source, and Molecular Foundary, Lawrence Berkeley National Laboratory, which was supported by the DOE, Office of Science, and Office of Basic Energy Sciences.

Received: May 6, 2015
Revised: August 15, 2015
Published online: October 1, 2015

[1] Z. C. He, C. M. Zhong, S. J. Su, M. Xu, H. B. Wu, Y. Cao, *Nat. Photon.* **2012**, *6*, 591.
[2] K. Zhang, C. M. Zhong, S. J. Liu, C. Mu, Z. K. Li, H. Yan, F. Huang, Y. Cao, *ACS Appl. Mat. Interfaces* **2014**, *6*, 10429.
[3] J. B. You, L. T. Dou, K. Yoshimura, T. Kato, K. Ohya, T. Moriarty, K. Emery, C. C. Chen, J. Gao, G. Li, Y. Yang, *Nat. Commun.* **2013**, *4*, 1446.
[4] W. W. Li, A. Furlan, K. H. Hendriks, M. M. Wienk, R. A. J. Janssen, *J. Am. Chem. Soc.* **2013**, *135*, 5529.
[5] Y. Li, *Acc. Chem. Res.* **2012**, *45*, 723.
[6] J. Chen, Y. Cao, *Acc. Chem. Res.* **2009**, *42*, 1709.
[7] J. Warnan, C. Cabanetos, A. El Labban, M. R. Hansen, C. Tassone, M. F. Toney, P. M. Beaujuge, *Adv. Mater.* **2014**, *26*, 4357.
[8] H. Kim, B. H. Lee, K. C. Lee, G. Kim, J. Y. Yu, N. Kim, S. H. Lee, K. Lee, *Adv. Energy Mater.* **2013**, *3*, 1575.
[9] C. Cabanetos, A. El Labban, J. A. Bartelt, J. D. Douglas, W. R. Mateker, J. M. Frechet, M. D. McGehee, P. M. Beaujuge, *J. Am. Chem. Soc.* **2013**, *135*, 4656.
[10] A. T. Yiu, P. M. Beaujuge, O. P. Lee, C. H. Woo, M. F. Toney, J. M. Frechet, *J. Am. Chem. Soc.* **2012**, *134*, 2180.
[11] T. Lei, J. H. Dou, J. Pei, *Adv. Mater.* **2012**, *24*, 6457.
[12] P. M. Beaujuge, J. M. Frechet, *J. Am. Chem. Soc.* **2011**, *133*, 20009.
[13] J. M. Szarko, J. Guo, Y. Liang, B. Lee, B. S. Rolczynski, J. Strzalka, T. Xu, S. Loser, T. J. Marks, L. Yu, L. X. Chen, *Adv. Mater.* **2010**, *22*, 5468.
[14] L. Q. Yang, H. X. Zhou, W. You, *J. Phys. Chem. C* **2010**, *114*, 16793.
[15] C. Piliego, T. W. Holcombe, J. D. Douglas, C. H. Woo, P. M. Beaujuge, J. M. J. Frechet, *J. Am. Chem. Soc.* **2010**, *132*, 7595.
[16] J. Mei, Z. Bao, *Chem. Mater.* **2014**, *26*, 604.
[17] J. Mei, D. H. Kim, A. L. Ayzner, M. F. Toney, Z. Bao, *J. Am. Chem. Soc.* **2011**, *133*, 20130.
[18] H. B. Akkerman, S. C. B. Mannsfeld, A. P. Kaushik, E. Verploegen, L. Burnier, A. P. Zoombelt, J. D. Saathoff, S. Hong, S. Atahan-Evrenk, X. Liu, A. Aspuru-Guzik, M. F. Toney, P. Clancy, Z. Bao, *J. Am. Chem. Soc.* **2013**, *135*, 11006.
[19] A. El Labban, J. Warnan, C. m. Cabanetos, O. Ratel, C. Tassone, M. F. Toney, P. M. Beaujuge, *ACS Appl. Mat. Interfaces* **2014**, *6*, 19477.
[20] J. Lee, M. Kim, B. Kang, S. B. Jo, H. G. Kim, J. Shin, K. Cho, *Adv. Energy Mater.* **2014**, *4*, 1400087.
[21] I. Osaka, M. Saito, T. Koganezawa, K. Takimiya, *Adv. Mater.* **2014**, *26*, 331.
[22] I. Osaka, Y. Houchin, M. Yamashita, T. Kakara, N. Takemura, T. Koganezawa, K. Takimiya, *Macromolecules* **2014**, *47*, 3502.
[23] K. R. Graham, C. Cabanetos, J. P. Jahnke, M. N. Idso, A. El Labban, G. O. Ngongang Ndjawa, T. Heumueller, K. Vandewal, A. Salleo, B. F. Chmelka, *J. Am. Chem. Soc.* **2014**, *136*, 9608.
[24] S. W. Ko, E. Verploegen, S. Hong, R. Mondal, E. T. Hoke, M. F. Toney, M. D. McGehee, Z. N. Bao, *J. Am. Chem. Soc.* **2011**, *133*, 16722.
[25] M. Wang, X. W. Hu, P. Liu, W. Li, X. Gong, F. Huang, Y. Cao, *J. Am. Chem. Soc.* **2011**, *133*, 9638.
[26] T. B. Yang, M. Wang, C. H. Duan, X. W. Hu, L. Huang, J. B. Peng, F. Huang, X. Gong, *Energy Environ. Sci.* **2012**, *5*, 8208.
[27] I. Osaka, T. Abe, M. Shimawaki, T. Koganezawa, K. Takimiya, *ACS Macro Lett.* **2012**, *1*, 437.
[28] T. B. Yang, M. Wang, Y. Cao, F. Huang, L. Huang, J. B. Peng, X. Gong, S. Z. D. Cheng, Y. Cao, *Adv. Energy Mater.* **2012**, *2*, 523.
[29] I. Osaka, M. Shimawaki, H. Mori, I. Doi, E. Miyazaki, T. Koganezawa, K. Takimiya, *J. Am. Chem. Soc.* **2012**, *134*, 3498.
[30] Y. M. Sun, J. Seifter, M. Wang, L. A. Perez, C. Luo, G. C. Bazan, F. Huang, Y. Cao, A. J. Heeger, *Adv. Energy Mater.* **2014**, *4*, 1301601.
[31] X. Hu, C. Yi, M. Wang, C.-H. Hsu, S. Liu, K. Zhang, C. Zhong, F. Huang, X. Gong, Y. Cao, *Adv. Energy Mater.* **2014**, *4*, 1400378.
[32] W. T. Li, L. Q. Yang, J. R. Tumbleston, L. Yan, H. Ade, W. You, *Adv. Mater.* **2014**, *26*, 4456.
[33] J. A. Bartelt, J. D. Douglas, W. R. Mateker, A. E. Labban, C. J. Tassone, M. F. Toney, J. M. Fréchet, P. M. Beaujuge, M. D. McGehee, *Adv. Energy Mater.* **2014**, *4*.
[34] R. J. Kline, D. M. DeLongchamp, D. A. Fischer, E. K. Lin, L. J. Richter, M. L. Chabinyc, M. F. Toney, M. Heeney, I. McCulloch, *Macromolecules* **2007**, *40*, 7960.
[35] S. Q. Zhang, L. Ye, W. C. Zhao, D. L. Liu, H. F. Yao, J. H. Hou, *Macromolecules* **2014**, *47*, 4653.
[36] H. Huang, N. J. Zhou, R. P. Ortiz, Z. H. Chen, S. Loser, S. M. Zhang, X. G. Guo, J. Casado, J. T. L. Navarrete, X. G. Yu, A. Facchetti, T. J. Marks, *Adv. Funct. Mater.* **2014**, *24*, 2782.
[37] J.-L. Bredas, *Mater. Horiz.* **2014**, *1*, 17.
[38] A. Hexemer, W. Bras, J. Glossinger, E. Schaible, E. Gann, R. Kirian, A. MacDowell, M. Church, B. Rude, H. Padmore, *J. Phys: Conf. Ser.* **2010**, *247*, 012007.
[39] E. Gann, A. Young, B. Collins, H. Yan, J. Nasiatka, H. Padmore, H. Ade, A. Hexemer, C. Wang, *Rev. Sci. Instrum.* **2012**, *83*, 045110.
[40] K. Zhang, X. Guan, F. Huang, Y. Cao, *Acta Chim. Sin.* **2012**, *70*, 2489.
[41] S. J. Liu, Z. P. Zhang, D. C. Chen, C. H. Duan, J. M. Lu, J. Zhang, F. Huang, S. J. Su, J. W. Chen, Y. Cao, *Sci. China Chem.* **2013**, *56*, 1119.
[42] C. H. Hsieh, Y. J. Cheng, P. J. Li, C. H. Chen, M. Dubosc, R. M. Liang, C. S. Hsu, *J. Am. Chem. Soc.* **2010**, *132*, 4887.
[43] C. M. Zhong, S. J. Liu, F. Huang, H. B. Wu, Y. Cao, *Chem. Mater.* **2011**, *23*, 4870.
[44] Y. Dong, X. W. Hu, C. H. Duan, P. Liu, S. J. Liu, L. Y. Lan, D. C. Chen, L. Ying, S. J. Su, X. Gong, F. Huang, Y. Cao, *Adv. Mater.* **2013**, *25*, 3683.
[45] M. Lenes, L. J. A. Koster, V. D. Mihailetchi, P. W. M. Blom, *Appl. Phys. Lett.* **2006**, *88*, 243502.
[46] M. S. Kim, B. G. Kim, J. Kim, *ACS Appl. Mat. Interfaces* **2009**, *1*, 1264.
[47] J. Nelson, *Phys. Rev. B* **2003**, *67*, 155209.
[48] Y. Liu, J. Zhao, Z. Li, C. Mu, W. Ma, H. Hu, K. Jiang, H. Lin, H. Ade, H. Yan, *Nat. Commun.* **2014**, *5*, 5293.
[49] Y. F. Li, Y. Cao, J. Gao, D. L. Wang, G. Yu, A. J. Heeger, *Synth. Met.* **1999**, *99*, 243.
[50] L. J. Huo, J. H. Hou, H. Y. Chen, S. Q. Zhang, Y. Jiang, T. L. Chen, Y. Yang, *Macromolecules* **2009**, *42*, 6564.
[51] Q. Hou, Q. M. Zhou, Y. Zhang, W. Yang, R. Q. Yang, Y. Cao, *Macromolecules* **2004**, *37*, 6299.
[52] Y. Zhang, K. Tajima, K. Hirota, K. Hashimoto, *J. Am. Chem. Soc.* **2008**, *130*, 7812.
[53] S. Mataka, K. Takahashi, Y. Ikezaki, T. Hatta, A. Torii, M. Tashiro, *Bull. Chem. Soc. Jpn.* **1991**, *64*, 68.